Half-integer-spin quadrupolar nuclei in magic-angle spinning paramagnetic NMR: The case of NaMnO2

José P Carvalho, Wassilios Papawassiliou, Andrew J Pell

Half-integer-spin quadrupolar nuclei in magic-angle spinning paramagnetic NMR: The case of $NaMnO_2$

José P. Carvalho[a,], Wassilios Papawassiliou,[a,], Andrew J. Pell[a,b,]

[a]*Department of Materials and Environmental Chemistry, Stockholm University, Svänte Arrhenius väg 16 C 106 91 Stockholm, Sweden*
[b]*Centre de RMN Très Hauts Champs de Lyon (UMR5082 - CNRS, ENS Lyon, UCB Lyon 1), Université de Lyon, 5 rue de la Doua, 69100 Villeurbanne, France.*

Abstract

A combination of solid-state NMR methods for the extraction of ^{23}Na shift and quadrupolar parameters in the as-synthesized, structurally complex $NaMnO_2$ Na-ion cathode material, under magic-angle spinning (MAS) is presented. We show that the integration of the Magic-Angle Turning experiment with Rotor-Assisted Population transfer (RAPT) can be used both to identify shifts and to extract a range of magnitudes for their quadrupolar couplings. We also demonstrate the applicability of the the two-dimensional one pulse (TOP) based double-sheared Satellite Transition Magic-Angle Spinning (TOP-STMAS) showing how it can yield a spectrum with separated shift and second-order quadrupolar anisotropies, which in turn can be used to analyze a quadrupolar lineshape free of anisotropic bulk magnetic susceptibility (ABMS) induced shift dispersion and determine both isotropic shift and quadrupolar products. Combining all these experiments, the shift and quadrupolar parameters for all observed Na environments were extracted and yielded excellent agreement with the density functional theory (DFT) based models that were reported in previous literature. We expect these methods to open the door for new possibilities for solid-state NMR to probe half-integer quadrupolar nuclei in paramagnetic materials and other systems exhibiting large shift dispersion.

Keywords: Paramagnetic NMR, Solid-state NMR, Magic-angle spinning, Quadrupolar interaction, TOP-STMAS, RAPT, MAT;

Email address: andrew.pell@mmk.su.se (Andrew J. Pell)

1. Introduction

Solid-state NMR (ssNMR) has become an established tool to study a wide range of systems in chemistry, physics, materials science and biology [1–9], due to it's ability to provide in-depth information regarding the local environments of a structure compared to diffraction methods that generally rely on long-range order [10]. Furthermore, ssNMR can also provide a site-specific insight into the electronic structure which makes it an effective method to study metallic materials, non-trivial insulators, and systems containing paramagnetic metal ions [11–14]. In the case of paramagnetic systems, the hyperfine interaction between the observed nucleus and the unpaired electrons gives rise to large spectral shifts and shift anisotropies which can provide information on the bonding geometry, spin-density and particle shape [15]. However, it can also render the acquisition and interpretation of the NMR spectra a more delicate process, as it may introduce (i) extremely large shifts and shift anisotropies (SA) that are difficult to excite using conventional methods, (ii) paramagnetic relaxation enhancements (PRE) which broaden the spectral lineshapes and causes the excited coherences to decay more rapidly [16] and (iii) bulk magnetic susceptibility (BMS) effects that may also give rise to additional line broadening [17, 18].

Very-fast spinning (MAS) has been shown to be key in overcoming the aforementioned obstacles, since it permits differentiation between several nuclear environments with different isotropic shifts [19, 20]. In addition, recently developed broadband pulse schemes that permit the manipulation of spin systems with both large shift dispersions and large anisotropic interactions, including the variable offset cumulative spectroscopy (VOCS) [21–24], and pulse sequences that employ short high-power pulses [20, 25, 26], have successfully been applied. Expanding upon this idea, the Magic-Angle Turning (MAT) [27, 28], Phase-Adjusted Spinning Sidebands (PASS) [29] and MATPASS [30, 31] experiments have been employed, to remove the overlap between spinning-sideband manifolds and extract the SAs. Further improvements have been achieved with the use of frequency-swept adiabatic pulses under both static and in MAS conditions [32–44] for increased bandwidth.

For quadrupolar nuclei (spin $I > 1/2$), the quadrupolar interaction arising from the coupling between the electrical field gradient (EFG) tensor at the nucleus position and the quadrupolar moment also may potentially introduce additional difficulties. The magnitude of this interaction can be quite extensive resulting in severe broadening of the spectral resonances [8]. However, similarly to the hyperfine interaction, the dependence on the EFG results in the quadrupolar parameters having a close link with crystal symmetry, local environment and dynamics [8], which, in turn, also causes it to be a valuable source of information.

Development of methods that are suitable for probing quadrupolar nuclei in paramagnetic systems has been more obscure contrary to their spin $1/2$ counterparts. The presence of a moderate-to-large quadrupolar interactions in conjunction with large paramagnetic shift anisotropies and BMS effects makes uniform excitation or inversion more difficult and complicates the extraction of the NMR parameters.

Notable pulse schemes have been proposed for integer quadrupolar systems such as the application of the Delays Alternating with Nutation for Tailored Excitation (DANTE) [45] to achieve broadband inversion and excitation, and the low-power excitation of double-quantum coherences in spins subject to large quadrupolar interactions [46, 47]. Pulse sequences designed for the separation separation of shift and quadrupolar interaction have also been proposed, for static samples the shifting $p-$echo [48], shifting $d-$echo [49], adiabatic shifting d-echo [50], and, more recently phase adjusted spinning sideband (PASS) [51] for spinning samples.

For half-integer quadrupolar nuclei in paramagnetic systems we have the additional problem of differentiating between the central transition (CTs) of different environments, and their accompanying satellite transitions (STs), both of which are broadened by the paramagnetic SA and are generally seen under high-power conditions used to obtain the spectrum. The most widely used method of achieving high-resolution, the multiple-quantum magic angle spinning experiment (MQMAS) [52], has not been widely successfully applied to paramagnetic systems, likely due to the interference between paramagnetic and quadrupolar effects. A rival experiment, the satellite transition magic angle spinning experiment (STMAS) [53], however, has been successfully applied to systems with low concentrations of a paramagnetic dopant ion and when combined a double shearing transformation based on the two-dimensional one pulse (TOP) scheme [54–57], yields a spectrum where shift and quadrupolar interactions are separated. Alternatively, the rotor-assisted population transfer (RAPT) method [58–60] has some success at estimating the quadrupolar parameters in paramagnetic systems [60].

In this work, we explore the performance and limitations of the state-of-the-art methods for extraction of both quadrupolar shift anisotropy tensor parameters in an as-synthesized $NaMnO_2$ system, which belongs to a class of layered sodium intercalation compounds that have been a focus of recent studies due to its applications as high-capacity Na-ion cathodes [61–64]. The complexity of $NaMnO_2$ stems from the fact that it may crystallize into several polymorphs. The assignment and validation of the proposed models for the structure of $NaMnO_2$ by Clément et al. [65] have hitherto been made solely based on a comparison of experimental isotropic shifts with DFT-calculated values. However, useful NMR parameters, such as the shift-anisotropy (SA) and quadrupolar interaction parameters, are not routinely used, despite containing potentially useful additional information. This is largely due to the difficulty in obtaining reliable experimental values, particularly for the quadrupolar parameters where the second-order spectral lineshapes are smeared out by paramagnetic line broadening.

This paper explores how far the current state-of-the-art experimental methods can be used to identify the different CTs and STs from different environments, obtain both isotropic shifts and quadrupolar tensor parameters for the different local environments, and how this additional information may be used to obtain a more detailed picture of the different struc-

tures within this complex paramagnetic material. More specifically, we will employ a combination of Hahn-echo and MAT experiments in conjunction with RAPT for site identification and coarse determination of the quadrupolar couplings. Subsequently, we refine our analysis via the TOP-STMAS experiment, for differentiation of the contributions from shifts and second-order quadrupolar effects, and ensuingly by fitting the slices of the MAT spectra, for extraction of the full NMR tensor parameters. Lastly, using the obtained parameters, we fit the Hahn-echo spectra acquired at two different external magnetic fields, to obtain an unambiguous assignment, and quantify the different sodium environments.

2. Experimental and Simulation Details

2.1. Synthesis procedure

The synthetic procedure was carried out based on previous literature[64, 66]. Appropriate amounts of Na_2CO_3 and Mn_2O_3 were mixed and ground to account for the evaporation of Na_2O during the firing process. The samples were then fired up under oxygen at 950° in two separate steps for 24 hours each. After those steps, the samples were quickly quenched to room temperature and placed inside an Ar-filled glovebox, due to air sensitivity.

2.2. Powder X-ray diffraction

Powder X-ray diffraction was performed on a Panalytical X'Pert PRO diffractometer operated with Cu-K_{α_1} radiation and in θ - 2θ diffraction geometry. Diffraction patterns were measured in a 2θ range of 5-90 °. Subsequent Rietveld analysis was performed with the software FullProf Suite [67].

2.3. Solid-state NMR

The solid-state NMR spectra were acquired on a 500 Avance NEO spectrometer and on a 600 Avance III Bruker spectrometer, at magnetic fields of 11.7 and 14.1 T, corresponding to Larmor frequencies of 132.294 and 158.744 MHz for ^{23}Na, respectively. In both cases 1.3 mm HX probes were used at 60 kHz MAS frequency. Both the ^{23}Na shifts and RF field strength were calibrated on solid NaCl, with ^{23}Na signal referenced at 7.21 ppm. At 11.7 T, all pulses were applied with a RF field strength with 225 kHz, corresponding to 0.56 and 1.11 μs $\pi/2$ and π CT selective pulses. RAPT pulses [68] operated at 159 kHz nutation frequency. At 14.1 T, all pulses operated with an RF field strength with a nutation frequency of 195 kHz, corresponding to 0.64 and 1.28 μs $\pi/2$ and π CT selective pulses.

In the discussion that follows, the observed ^{23}Na shifts are defined as

$$\delta_{\text{obs}} = \delta_{\text{iso}} + \delta_{\text{QIS}}, \tag{1}$$

where δ_{QIS} is the second-order isotropic quadrupolar induced shift given by

$$\delta_{\text{QIS}} = A^0(I,q)\left[\frac{3}{4I(2I+1)}\right]^2 \frac{P_q^2}{\nu_0}, \tag{2}$$

where ν_0 is the Larmor frequency, δ_{iso} the isotropic shift, P_q the quadrupolar product,

$$P_q = C_q\sqrt{1+\frac{\eta_q^2}{3}}, \tag{3}$$

and $A^0(I,q)$ is a spin (I) and transition (q) dependent coefficient [69]. C_q is the quadrupolar coupling given by

$$C_q = \frac{e^2qQ}{2I(2I-1)}, \tag{4}$$

where eQ is the nuclear quadrupole moment and eq is the zz component of the electrical field gradient (EFG) tensor, $\tilde{V}_{ii}$ in the principal axis frame (PAF). The components of the EFG in the PAF are ordered as $\left|\tilde{V}_{zz}\right| \geq \left|\tilde{V}_{yy}\right| \geq \left|\tilde{V}_{xx}\right|$. The quadrupolar splitting frequency ω_q and asymmetry parameter η_q are defined as

$$\omega_q = \frac{3\pi C_q}{2I(2I-1)}, \tag{5}$$

$$\eta_q = \frac{\tilde{V}_{xx}-\tilde{V}_{yy}}{\tilde{V}_{zz}}. \tag{6}$$

The shift tensor is characterized by the three principal components that are ordered according to the Haeberlen convention, $\left|\tilde{\delta}_{zz}-\delta_{\text{iso}}\right| \geq \left|\tilde{\delta}_{xx}-\delta_{\text{iso}}\right| \geq \left|\tilde{\delta}_{yy}-\delta_{\text{iso}}\right|$ where

$$\delta_{\text{iso}} = \frac{1}{3}\left(\tilde{\delta}_{xx}+\tilde{\delta}_{yy}+\tilde{\delta}_{zz}\right) \tag{7}$$

and $\tilde{\delta}_{xx}$, $\tilde{\delta}_{yy}$ and $\tilde{\delta}_{zz}$ are the components of the shift tensor in the PAF and δ_{iso} the isotropic shift. The shift anisotropy (SA), $\Delta\delta$, and asymmetry parameter, η, are given by,

$$\Delta\delta = \tilde{\delta}_{zz} - \delta_{\text{iso}} \tag{8}$$

$$\eta = \frac{\tilde{\delta}_{yy}-\tilde{\delta}_{xx}}{\Delta\delta}. \tag{9}$$

We note that SA corresponds to a generalization of the chemical shift anisotropy (CSA) to include the contribution from unpaired electrons. For ^{23}Na, the orbital contributions [70] to the SA tensor are generally negligible.

RAPT pulse trains applied prior to a rotor-synchronised Hahn-echo sequence, using $x - \bar{x}$ pulses, as shown in figure 2(a), saturate the populations of the satellite transitions (STs) so that their net polarization reduced to zero and, consequentially, yields a sensitivity enhancement of the central transition (CT) signal by a factor of $I + 1/2$, where I corresponds to the nuclear spin which for ^{23}Na is 3/2, giving a maximum theoretical enhancement of 2 [60]. The repetition frequency, defined as $\nu = 1/(2\tau_1)$, where τ_1 is the interpulse delay, corresponding to an experimental setup that gives the largest enhancement when ν is equal to the quadrupolar splitting frequency [58–60, 71–73],

$$\nu = \frac{\omega_q}{2\pi}. \tag{10}$$

The maximum enhancement is, therefore, independent of η_q. The enhanced CT polarization is then excited using a conventional Hahn-echo sequence, as shown in figure 2(a), and corresponds to an enhanced signal.

The one-dimensional spectra shown in figure 3(a) was acquired with a RAPT pulse train with 20 loops, 525 kHz repetition frequency and using 4096 scans and 125 ms recycle delay. The experimental signal enhancements shown figure 4 were measured by varying the repetition frequency in a total of 27 steps of 25 kHz (from 250 kHz to 900 kHz), accumulating 2048 transients per frequency step and using 125 ms recycle delay. The enhancement profiles were benchmarked on the four-coordinate ^{27}Al resonance of yttrium aluminium garnet (see figure 1 of the SI).

The 2D MAT [27] experiment, shown in figure 1(b), uses a sequence of 5 π-pulses to manipulate the spinning sidebands and separate them by isotropic shift in the indirect dimension. The spectrum was recorded with a recoupling time of two rotor periods and 128 complex increments (480 kHz spectral width in the indirect dimension), 2800 scans per increment and a recycle delay of 33 ms. The MAT pulse sequenced was preceded by a RAPT pulse train identical to that used for the one-dimensional spectrum.

The TOP-STMAS experiment was performed using the z-filtered STMAS pulse sequence [57, 69] as shown in figure 1(c), preceded by a simple saturation pulse train for preparation of the magnetization. This experiment uses the fact that the transition pathway that goes through a satellite transition (ST) during t_1 and ends on the CT in t_2, does not form simultaneous echoes for the isotropic nuclear shielding, isotropic quadrupolar and anisotropic quadrupolar contributions, as shown in Figure 3 of the SI, and only after double-shearing transformation the isotropic shift and quadrupolar anisotropy is separated into orthogonal dimensions [57, 74, 75]. Here, we employed a TOP-based protocol [54–56, 76], by carrying out active shearing transformations of the discretely-sampled-data, exploiting the Fourier shift theorem [77], after the generation of all four time-domain quadrants, and by swapping the direct and indirect dimensions, as described in Carvalho et al. [57] (see Figure 3 of the SI for a schematic of STMAS time-domains before and after the shearing transformations). The center-of-gravity of the lineshape in each dimension is given by

$$\delta_{\text{Shift}} = \delta_{\text{iso}} + \delta_q \cdot SC_{\delta_{q,1}}, \tag{11}$$

$$\delta_{\text{Quad}} = \delta_q \cdot SC_{\delta_{q,2}}, \tag{12}$$

where

$$\delta_q = \left[\frac{3}{4I(2I+1)}\right]^2 \frac{P_q^2}{\nu_0}, \tag{13}$$

and $SC_{\delta_{q,1/2}}$ corresponds to the quadrupolar shift coefficients, given in Ref. [57]. Along the quadrupolar dimension, the lineshapes can be analyzed without shift-dispersion induced broadening arising from ABMS effects. The STMAS spectrum, will also exhibit a CT-CT and ST-ST diagonal peaks, with the latter generally being negligible, that form echoes simultaneous with the isotropic nuclear shielding and thus appear at $\delta_{\text{Quad}} = 0$, since these pathways cannot be filtered via phase-cycling. The time-dependent contributions of the chemical shift anisotropy and quadrupolar interactions are refocused along the time-dependent echo ridge represented in figure 2 of the SI. After the double shearing transformation these contributions appear in both dimensions. The spectra shown in figure 5 was recorded employing 1.35 μs pulse for both the excitation and reconversion of the satellite coherences and 0.56 μs for the final CT selective pulse. 256 complex increments were recorded with a sampling interval of 16.67 μ in t_1 and 2048 transients per increment using a 33 ms recycle delay using the States–Haberkorn–Rubens method [78].

The final one-dimensional MAS spectra were recorded using a two-rotor period synchronised Hahn-echo sequence. At 11.7 T external magnetic field, 32768 transients were accumulated with a relaxation delay of 125 ms to ensure quantitative results. In table 1 of the SI the T_2' coherence lifetime and T_1 spin-lattice relaxation time, determined using rotor synchronised Hahn-echo and echo-detected saturation recovery, respectively, are shown for each observed site. At 14.1 T, 65536 transients were accumulated with a relaxation delay of 50 ms.

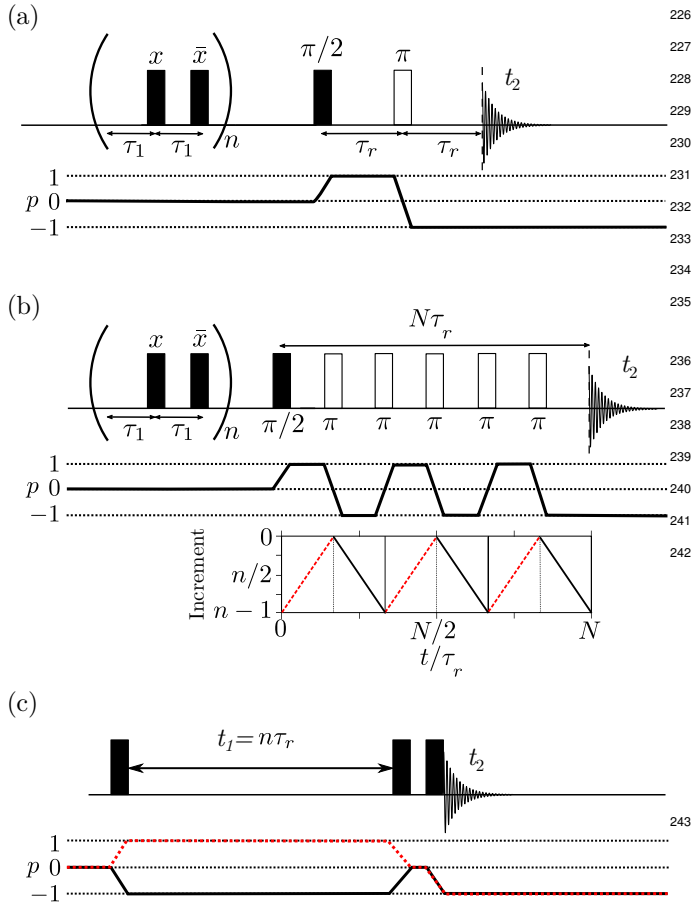

Figure 1: Pulse sequences and coherence transfer pathways (CTP) for the experiments used to extract shifts and quadrupolar parameters: (a) Rotor-synchronised Hahn echo sequence preceded by a train of $x\bar{x}$ pulses for RAPT with repetition frequency given by $\nu = 1/(2\tau_1)$. (b) Five π-pulse MAT pulse sequence also preceded by a RAPT train, with an evolution time of N rotor periods, where N is an integer that is not a multiple of 3. Pulses at $(2/6)N\tau_r$ and $(4/6)N\tau_r$ are fixed and the timings of the remaining π pulses are shifted according to echo or anti-echo types as shown in the pulse-timings below, where n is the number of increments acquired in the indirect dimension. (c) z -filtered STMAS experiment where dashed red and black pathways correspond to the N-type and P-type datasets. n is incremented from 1 in steps of a single rotor period. A representation of the STMAS time-domains before and the TOP based double-shear transformation is shown in figure 2 of the SI. All $\pi/2$ and π correspond to CT selective pulses.

2.4. Simulations

Numerical simulations of the NMR spectra were all performed using SIMPSON [79] considering 579 crystallite orientations using the Alderman, Solum, Grant (ASG) scheme [80]. The quadrupolar and CSA parameters were obtained by fitting slices of the MAT spectra including only the contribution arising only from the CT and 20 γ angles. Constraints on $|C_q|$ and on δ_{iso} for one of the sodium environments were imposed in accordance with the results of the TOP-STMAS spectrum and RAPT signal enhancement curves. The errors of the fitted parameters where determined using Monte-Carlo error estimation as described in Aleksis et al. [50].

RAPT buildup curves were obtained by first fitting the one-dimensional spectrum acquired with a RAPT pulse train with repetition frequency of 525 kHz, using six mixed Gauss-Lorentz functions for the centerband of each observed resonance. Each slice of the buildup pseudo-2D spectrum together with the one-dimensional spectrum acquired without the RAPT pulse train were then also fitted using the fitting function, allowing only the parameters governing the signal intensity to vary. The enhancement ratios were obtained considering the intensities of the one-dimensional spectra and subsequentially used to normalize the buildup data. The buildup curves were smoothed using a moving-average filter to mitigate the impact of the noise.

The final one-dimensional MAS spectra were fitted simply by allowing the intensity arising from the CT and STs of each site to vary, with fixed NMR parameters. The contribution of the signals from the satellite transition was constrained to never exceed the maximum theoretical intensity ratio with respect to the central transition. Each one-dimensional lineshape was simulated in SIMPSON with 100 γ-angles.

3. Results and Discussion

Rietveld refinement of as-synthesized $NaMnO_2$, shown in figure 2 of the SI, revealed a ratio of roughly 62 : 18 : 20 of β (*Pmnm* space group, figure 2(a)), α (*C*2/*m* space group, figure 2(b)) and orthorhombic (*Cmcm* space group, figure 2(c)) phases. These results are consistent with the previous literature, since recent studies revealed that this system is normally composed of regions of ideal β and α phases due to their similar formation energies [64, 65]. Orthorhombic phases that correspond to distorted forms of the hexagonal P2 structures, with a $P6_3/mmc$ space group, have also been reported in the sodium deficient material $Na_{2/3}MnO_2$ [63]. The absence of a [101] reflection of the β form at 23.3° is indicative of a contribution of over 25% of stacking faults, which arise from intergrowth with α domains within the β phase [62]. These stacking faults were modeled by Clément et al. [65] via the construction of two structures termed mixed cells 1 and 2, containing twin boundaries between α and β domains, permitting the study of their inter-growth and computation sodium deintercalation potentials. The occurrence of these stacking faults has been ascribed to low interfacial energy between α and β forms $NaMnO_2$. Both cells encompassed representative local sodium environments in the twin boundaries of both phases, permitting the calculation of their respective NMR parameters, which served to validate of their findings.

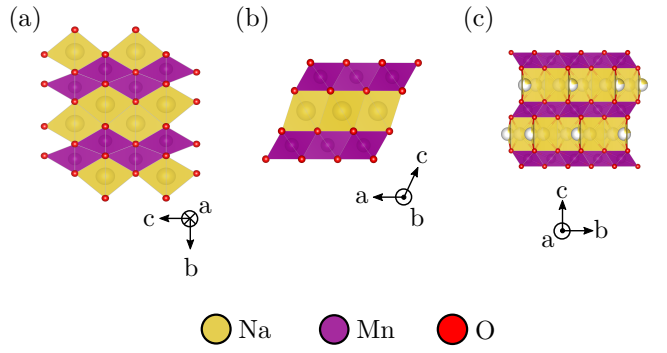

Figure 2: Crystal structure of the three forms of Na_xMnO_2: (a) orthorhombic β-$NaMnO_2$ in *Pmnm* space group exhibiting corrugated layers, (b) a Jahn-Teller distorted α-$NaMnO_2$ structure with a monoclinic $C2/m$ space group and (c) orthorhombic sodium deficient $Na_{2/3}MnO_2$ in *Cmcm* space group.

The one dimensional ^{23}Na spectra of $NaMnO_2$ with and without the application of a RAPT pulse train are shown in figure 3(a). The dominant NMR interactions in these systems are the quadrupolar couplings and hyperfine shifts. The latter can be divided into the isotropic Fermi contact shift, determined by the sum of the individual Mn-O-Na bond pathway shift contributions, sensitive to the oxidation state of the transition metal [81], and the spin-dipolar interaction, which dominates the SAs. We note that at lower sodium content, Na_xMnO_2, we expect higher sodium shifts, since the oxidation of Mn^{3+} to Mn^{4+} leads to a higher hyperfine shift [63–65].

As previously shown by Billaud et al. [64] the lineshape exhibits multiple ^{23}Na environments, with three clear distinct main resonances at 309, 500 and 830 ppm. These environments have been previously assigned to an ideal β-"like" environment, a sodium site in the vicinity of a stacking fault, and an α-"like" environment, respectively. The spectral lineshapes are also relatively broad due to a combination of structural disorder, ABMS and second-order quadrupolar effects.

The application of a RAPT pulse train yields an enhancement of approximately 1.4, corresponding to less than half of the maximum theoretical enhancement 2. Nevertheless, it is a useful tool to enhance CT signal-to-noise ratio while simultaneously suppressing the contributions from the satellites. Furthermore, evaluating the repetition frequency that yields the maximum enhancement for each site gives an estimate of the magnitude of their corresponding C_q. Since we are in the presence of multiple sodium environments, we first need to separate the overlapping spinning sideband manifolds, in order to identify the different resonances.

The MAT experiment was only designed for spin systems with rank 2 SA broadening, since the time-dependent modulation of rank 4 terms, introduced by the second order quadrupolar interaction, are not refocused. Considering that the rank 2 interactions are much larger in magnitude and we are operating at a spinning frequency that is much larger than the width of the MAS lineshape, as clearly evidenced in the one-dimensional lineshapes shown in figure 3(a), and, therefore, with adjacent sidebands that do not overlap with each other, there is little justification version of MAT experiment that refocuses the contributions arising from the second order quadrupolar interaction [82–84].

In figure 3(b) the 2D MAT spectrum is shown exhibiting six distinct sodium peaks, including the three main resonances at 309, 500, 830 ppm, and additional, at lower intensity, that were not distinguishable in the 1D spectrum, at shifts of 356, 539 and 1170 ppm. The resonances at 356 and 539 ppm are attributed to sodium environments near the planar defects that have similar Mn-O-Na hyperfine interactions to the β and stacking fault environments observed by Billaud et al. [64], respectively, and, hence, similar Fermi contact shifts. These resonances, however, differ in the spatial arrangement of the atoms around the central sodium ion [65], which in turn correspond to differences in the observed shift of approximately 40 ppm in induced shift. Nevertheless, these environments are hard to distinguish in the experimental NMR spectrum since the inherent linewidth of the sodium resonances is roughly 20 ppm. Furthermore, since the separation between the satellite and central transition resonances considering the quadrupolar couplings reported in Billaud et al. [64] corresponds to roughly 40 ppm at an external magnetic field of 11.7 T, these sites also overlap with signal contributions arising from the STs of the main sites at 309 and 500 ppm. However, since we saturate the satellite transition populations with a RAPT train it is unlikely that contributions arising from STs would be significant. The resonance observed at 1170 ppm has also been reported in Clément et al. [65] in Na_xMnO_2 samples with low sodium content, $x \sim 0.4$, and was attributed to sodium environments in a different phase and local environment. This site likely arises from the presence of the orthorhombic sodium deficient phase revealed by XRD, also observed by Clément et al. [63], since higher sodium shift is consistent with the oxidation of Mn^{3+} to Mn^{4+}.

We proceed to investigate the enhancement factors of the observed resonances in the RAPT buildup curves, as shown in figure 4. The integrals were all evaluated considering the Gauss-Lorentz functions used to deconvolve the one-dimensional lineshape shown in 2(a). For each slice of the RAPT buildup curve, only the intensities of each Gauss-Lorentz function were allowed to vary, ensuring the effect of the overlap of the lineshapes was minimized. All six sites clearly show an enhancement of the signal intensity which further evidences that they correspond, predominantly, to CT lineshapes. Additionally, the maximum in the profiles permitted the estimation of a range of C_q values. It is worth noting that the ranges are of the order of 1 MHz which is relatively quite large, which reflects the limitations of the method to estimate $|C_q|$ accurately, particularly in the presence of overlapping resonances.

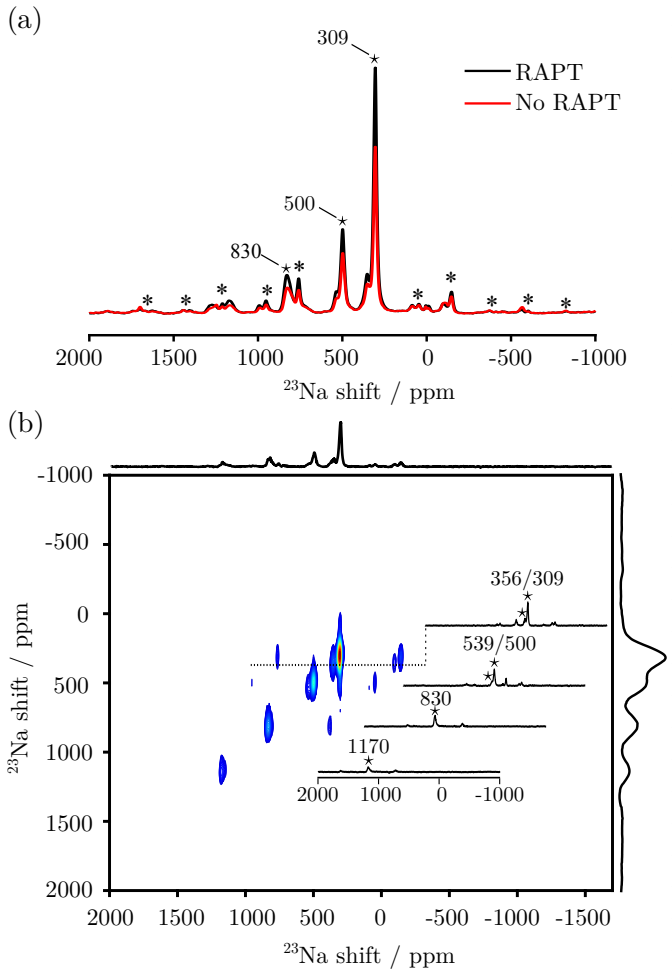

Figure 3: RAPT-enhanced ^{23}Na solid-state NMR spectra of $NaMnO_2$. (a) One-dimensional Hahn-echo spectrum of $NaMnO_2$ with and without the application of a RAPT pulse train illustrating the enhancement of the signal intensity of the central transition. Observed centerbands and sidebands marked with by stars ($\star$) and asterisks ($*$), respectively. (b) MAT spectrum of $NaMnO_2$ exhibiting six resonances with distinct observed shifts. Inset spectra correspond to extracted direct-dimension slices, and the observed shifts correspond to the centerbands marked by stars ($\star$). RAPT pulses were applied before the MAT experiment to enhance the signal-to-noise ratio and suppress the signals arising from the satellite transitions. Both spectra were recorded at 60 kHz MAS and at an 11.7 T external magnetic field. RAPT pulse trains were employed with a repetition frequency of 525 kHz.

In order to address the limitations of RAPT buildups in determining the quadrupolar interaction parameters, a 2D TOP-STMAS spectrum was acquired, shown in figure 5(a), which permitted the extraction of the quadrupolar products and isotropic shifts for the resonances observed at at 309 and 500 ppm, for which an ST-CT correlation cross-peaks is observed. The lineshapes along the quadrupolar dimension do not exhibit the features characteristic of quadrupolar lineshape, which indicates that a ABMS induced shift dispersion is not the only contributing factor to the smearing of its features. Since $NaMnO_2$ is significantly disordered system, its local environments likely exhibit a distribution of quadrupolar parameters and, consequentially, quadrupolar induced shifts, which result in broadening of the lineshape. Broadening effects arising from PRE are likely to also play a significant role. Nevertheless by fitting the extracted slices marked with dashed lines with Gauss-Lorentz functions we can determine the centers-of-gravity which can then be used to determine both isotropic shifts and quadrupolar products, using equations 11 and 12. Combining these results with the the range of quadrupolar couplings determined via the RAPT buildup and considering $0 \leq \eta_q \leq 1$, ranges of quadrupolar couplings of $2.4 - 2.9$ and $2.3 - 2.7$ MHz were estimated for the resonances observed at 309 and 500 ppm. Both represent a significant improvement upon the range predicted solely by the RAPT buildup curves. Moreover the TOP-STMAS allowed a separation of the isotropic shift δ_{iso} from the second-order quadrupolar shift. The isotropic shifts, δ_{iso}, were thus determined to be 325 ± 6 and 518 ± 7 ppm, respectively. While the peaks observed at 356 and 539 ppm only exhibit clear distinct CT-CT correlation diagonal peaks, since the contribution ST-ST correlation diagonal peaks is expected to be negligible, their presence constitutes additional evidence of that these observed resonances correspond, predominantly, to distinct sodium environments. The peak at 1170 ppm was not clearly discernible in the TOP-STMAS spectrum likely due to its lower overall intensity.

Considering the STMAS and RAPT buildup results, the slices of the MAT spectrum shown in 3(b) were fitted including only the CT taking into account the second-order quadrupolar and shift anisotropy interactions. Both the fitting constraints and starting condition were set to be in accordance the ranges of magnitude of the quadrupolar couplings and and the STMAS spectrum shown in figure 5. The fitted slices are shown in figure and in table 1(d) the extracted NMR parameters are compiled, together with the DFT predicted parameters for the α, β and mixed cells reported in ref. [65].

The NMR parameters for the resonance observed resonance at 309 ppm match remarkably well the parameters predicted for β-$NaMnO_2$. The site at 356 ppm arises from a β-like environment close to the planar defects, (Na(β)) in mixed cell 1. The agreement between the fitted and DFT predicted parameters is not as good as for the β environment, particularly in C_q which is slightly higher. We attribute this discrepancy to inherent difficulty of accurately fitting this resonance due to its proximity to the more intense β environment at 309 ppm. The resonances observed at 500 and 539 correspond to sites in the vicinity of the twin boundary (SF) and match reasonably well with intermediate sites Na(1) and Na(2) of mixed cell 1. Lastly, the site observed at 830 ppm was attributed to sodium in an α environment. This resonance was observed at a higher shift than previously reported, 751 ppm, which can be an indication of this local environment having a slightly lower sodium content leading to Mn^{3+} oxidation which would result in a higher overall Na shift. This increase in shift was also observed during the electrochemical cycle in Billaud et al. [64]. In spite of the shift difference, the NMR parameters extracted for this site are in good agreement with the parameters predicted for both pristine α-$NaMnO_2$ and the α-like environment, (Na(α)). The overall accordance of all NMR parameters, beyond the δ_{iso}, not only corroborates the DFT predictions for the pure α and β phases but also further validates the proposed models for the sodium environments in stacking faults between twin boundaries of α

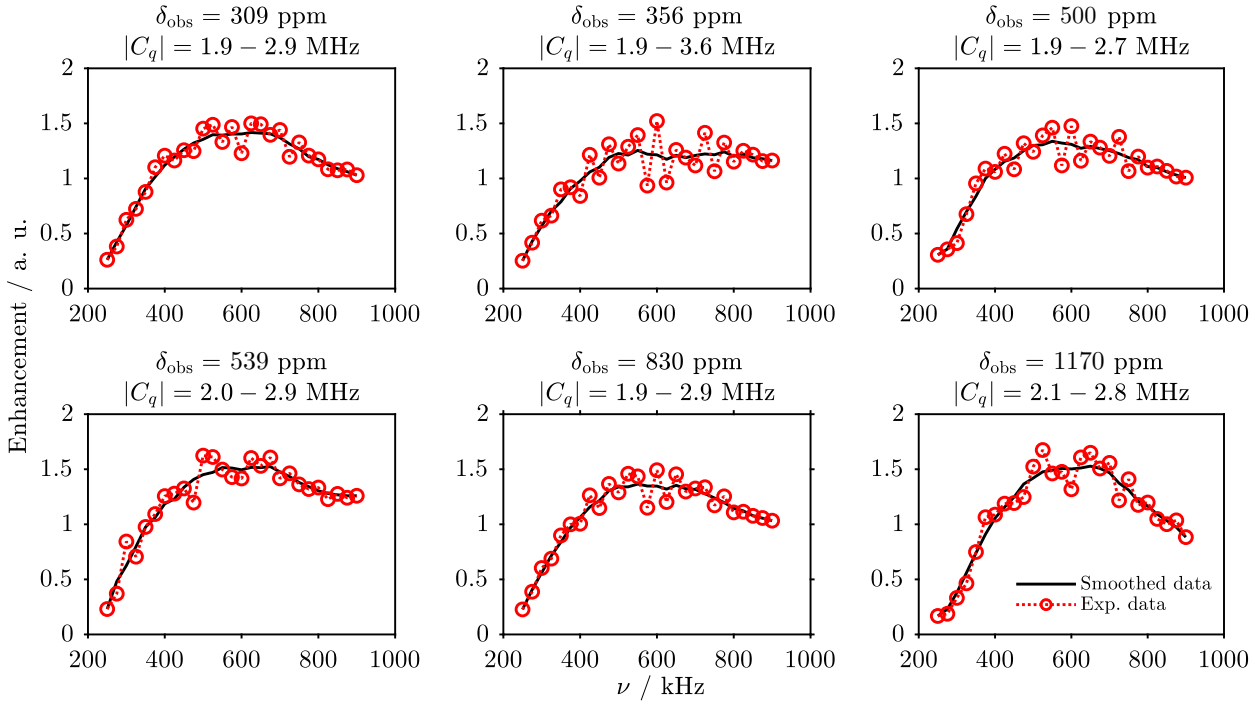

Figure 4: RAPT-enhancements for the six ^{23}Na resonances extracted from the MAT spectra with increasing repetition frequency of the RAPT pulses. The data points are indicated by red circles. The smooth black curves were obtained by employing a moving-average filter and were used to estimate the maximum enhancement factor. Considering frequency interval corresponding to ±5% of the maximum enhancement factor and using equation (10), the range of magnitudes of the quadrupolar couplings $|C_q|$ was determined.

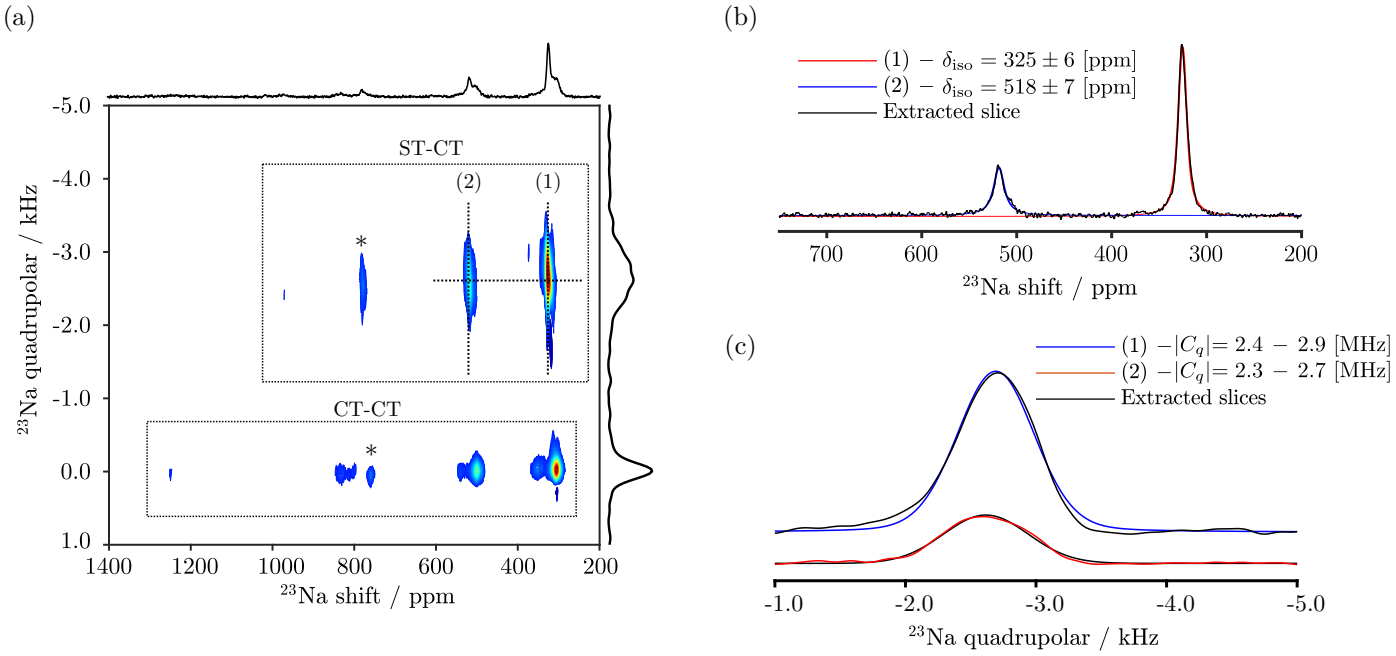

Figure 5: (a) Sheared z -Filtered TOP-STMAS spectrum showing the CT-CT diagonal peaks of five observed resonances, around 0 kHz in the indirect dimension, and the Satellite Transition (ST)-CT diagonal peak for the sites whose central transition is observed at 309 and 500 ppm, at around −2.6 kHz in the indirect dimension. Sidebands are marked with (⋆). Extracted slices along the shift and quadrupolar dimensions together with the best fits are shown in figures (b) and (c), respectively. The spectral lineshapes were all simulated considering Gauss-Lorentz curves whose centers-of-gravity were used to determine the quadrupolar products, P_q (3 ± 0.2 MHz for (1) and 3 ± 0.3 MHz for (2)), and isotropic shifts using equations (11) and (12). The STMAS spectrum was recorded while spinning at 60 kHz MAS and at 11.7 T.

and β phases. Lastly, the resonance observed at 1170 ppm, denoted Na*, is ascribed to local environments in the sodium deficient phase shown in figure 2(c).

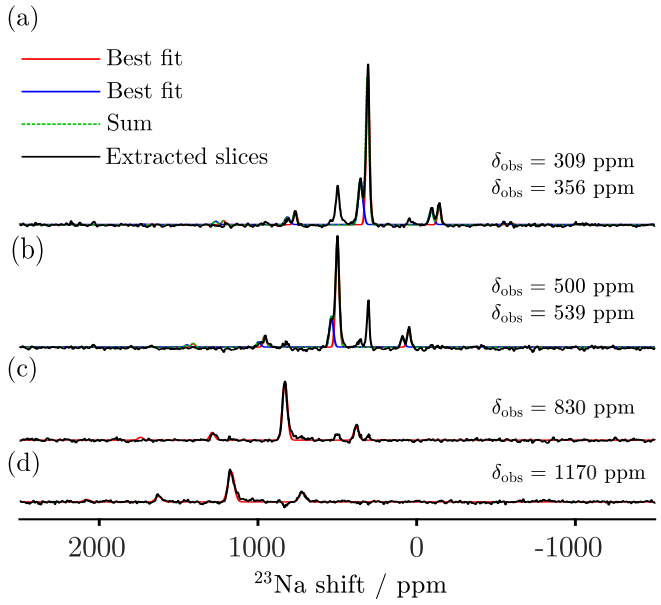

Figure 6: Extracted direct dimension slices from the MAT spectrum. Slices (a) and (b) were fitted considering two sodium environments, corresponding to the curves in blue and red, with the sum represented in dashed green, while the slices (c) and (d) were fitted with only one environment, corresponding to the curve in red. Experimental data points are represented in black. The fitting models included the second-order quadrupolar and shift anisotropy interactions and only included the CT. The magnitudes of the quadrupolar couplings $|C_q|$ were constrained to be in agreement with the RAPT build curves shown in figure 4 and the STMAS spectrum shown in figure 5. For slice (a) the isotropic chemical shift of the dominant resonance was further constrained to be in accordance with the STMAS spectrum. The observed shifts, $\delta_{obs} = \delta_{iso} + \delta_{QIS}$, were calculated using equation (2) for an external magnetic field of 11.7 T. The extracted shift and quadrupolar parameters are given in table 1. Additional details pertaining to the simulated lineshapes are given in the Experimental and Simulation Details section.

Fixing the obtained NMR parameters extracted from the MAT slices, shown in table 1, the one-dimensional fully relaxed Hahn-Echo spectrum recorded at 11.7 T, shown in figure 7(a), was fitted to obtain the relative quantifications of sodium environments (see table 1 of the SI for relaxation measurements). About 61% and 23% of Na nuclei are in β-like and stacking-fault like environments, respectively, and 8% are α-like and Na* environments. It is worthwhile to note that for this fit the contributions arising from both the CT and ST were included. As noted by Clément et al. [65], these results also suggest the presence of different stacking sequences, since structural models based purely on mixed cell 1 predict higher proportion of α-like environments than stacking-fault like environments, and models based purely on mixed cell 2 would result in more α-like environments. Nevertheless, considering the good the agreement between the NMR parameters of environments in the vicinity of the twin boundary and the Na(1) and Na(2) sites, the stacking sequences should be closer to those in mixed cell 1.

In order to verify the consistency of our model, Hahn-Echo spectrum recorded at 14.1 T was fitted using the same model, as shown in figure 7(b). Both lineshapes fit the experimental data considerably well. We also note that the Rietveld refinement of the diffraction pattern, shown in figure 1 of the SI, which indicated a 62 : 18 : 20 ratio between the β, α and distorted P2 phases, is also reasonable agreement with the quantification obtained using NMR.

4. Conclusions

We have presented a detailed structural investigation of an as-synthesized $NaMnO_2$ sample using state-of-the-art methods for paramagetic half-integer quadrupolar nuclei, showing how far these methods can go to extracting precise NMR parameters, and where they are limited. We show that using a conventional 5-π pulse MAT experiment enhanced by a RAPT saturation train applied beforehand we can separate the spinning sidebands and determine the observed shift positions. This information can in turn be used to carry out a more refined analysis of the RAPT buildup curves to extract a range of magnitudes of the quadrupolar coupling.

Using a TOP based double-shearing transformation we shown that we can effectively separate shift and second-order quadrupolar into orthogonal dimensions, which allows us to analyze slices in the quadrupolar dimension free of ABMS induced shift dispersion. Extracting the center of mass in both shift and quadrupolar dimensions we obtain the quadrupolar products and isotropic shifts.

Combining the information extracted via TOP-STMAS with the RAPT buildups, direct-dimension slices of the MAT spectrum can be fitted to extract the remaining shift and quadrupolar parameters. Very good agreement between extracted NMR parameters and the calculations reported in Clément et al. [65], which further validates their proposed models for the twin-boundaries of α and β type domains occurring in this system, using mixed α/β-$NaMnO_2$ structures. The fitting model was also used to accurately quantify the amount of sodium ions in each environment.

We anticipate that the methodology presented here will lay a blueprint for new studies of half-integer quadrupolar nuclei in paramagnetic systems and systems exhibiting large shift dispersion.

Declaration of Competing Interest

The authors declare that they have no known competing financial interests or personal relationships that could have appeared to influence the work reported in this paper.

Acknowledgements

This work was supported by the Swedish Research Council (2016-03441), and the Agence Nationale de la Recherche (ANR), through grant ANR-21-CE29-0010-01.

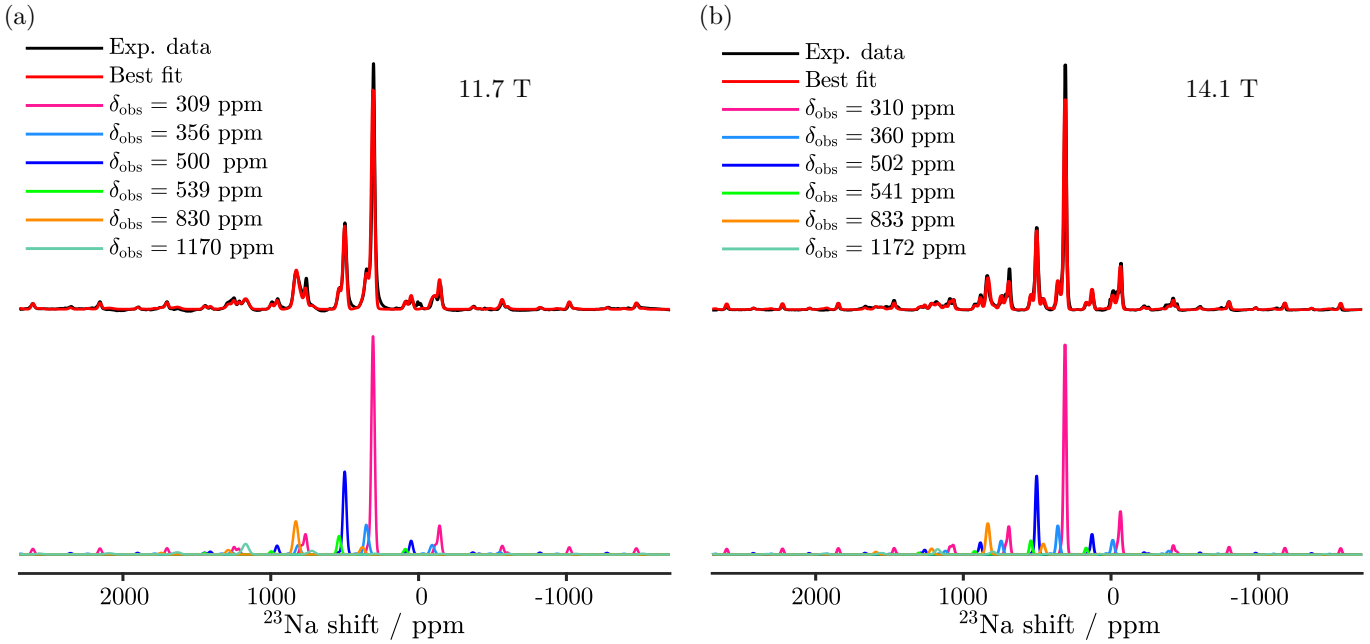

Figure 7: One-dimensional Hahn-echo ^{23}Na experimental spectra and best-fits of $NaMnO_2$ at 11.7 (a) and 14.1 T (b) both at 60 kHz MAS. The fitting model comprises of 6 distinct sodium sites, taking into account the contribution of both central and satellite transitions. All NMR parameters were fixed in accordance with the fitting models shown in figure 6, with corresponding NMR parameters given table 1. The total intensity of each site and relative intensity of the satellite transitions (ST) and central transition (CT) was allowed to vary. The relative intensity of the satellite transitions was constrained to never exceed their theoretical limit. The 14.1 T spectrum was fitted with the relative ST-to-CT intensities fixed intensity ratios set to match the 11.7 T data, and only the relative intensity of each site was allowed to vary. Taking into account the relative intensities of the spectrum recorded at 11.7 T, the relative quantification of each sodium environment was computed and is also given in table 1. The observed shifts, $\delta_{obs} = \delta_{iso} + \delta_{QIS}$, were calculated using equation (2) for the two different magnetic fields. The small peak at $\sim$ 0 ppm is due to a Na^+ in a residual diamagnetic impurity not predicted by the fitting model. Additional details pertaining to the simulated lineshapes are given in the Experimental and Simulation Details section.

DFT parameters: (a) α/β-$NaMnO_2$	Site	δ_{obs}	δ_{iso} [ppm]	$\Delta\delta$ [ppm]	η	C_q [MHz]	η_q
	β	51 – 372	61 – 388	509 – 585	0.63 – 0.78	2.53 – 3.04	0.38 – 0.86
	α	548 – 1099	567 – 1109	999 – 1139	0.17 – 0.19	−3.60 – −2.39	0.24 – 0.81
(b) Mixed cell 1							
	Na(β)	156 – 367	169 – 379	563 – 585	0.63 – 0.67	2.80 – 2.95	0.41 – 0.56
	Na(1)	392 – 692	404 – 704	−568 – 561	0.96 – 0.98	2.70 – 2.77	0.64 – 0.70
	Na(2)	454 – 761	469 – 776	991 – 1003	0.10 – 0.13	−2.83 – −2.77	0.99 – 1.00
	Na(α)	735 – 1165	750 – 1179	1077 – 1126	0.16 – 0.18	−2.89 – −2.81	0.83 – 0.87
(c) Mixed cell 2							
	pseudo β	184 – 426	199 – 441	877 – 897	0.05 – 0.07	2.85 – 2.88	0.89 – 0.92
	pseudo α	628 – 1085	640 – 1097	−666 – −617	0.60 – 0.67	2.60	0.85

(d) Experimental	Assignment	Obs. Shift	δ_{iso} [ppm]	$\Delta\delta$ [ppm]	η	$\lvert C_q \rvert$ [MHz]	η_q	Quantification [%]
	β_1	309 ± 6	319 ± 2	570 ± 60	0.2 ± 0.6	2.4 ± 0.2	0.9 ± 0.4	49 ± 1
	β_2	356 ± 8	378 ± 3	800 ± 100	0.9 ± 0.6	3.5 ± 0.2	0.9 ± 0.2	12 ± 2
	SF_1	500 ± 5	513 ± 3	630 ± 90	0.0 ± 0.5	2.7 ± 0.1	0.9 ± 0.2	19 ± 1
	SF_2	539 ± 8	554 ± 4	800 ± 900	0.0 ± 0.8	2.9 ± 0.1	0.9 ± 0.4	4 ± 1
	α	830 ± 10	843 ± 5	710 ± 90	0.0 ± 0.7	2.6 ± 0.4	0.9 ± 0.4	8 ± 1
	Na*	1170 ± 10	1181 ± 7	800 ± 100	0.0 ± 0.7	2.7 ± 0.6	0 ± 1	8 ± 1

Table 1: (a) Range of DFT predicted NMR parameters for α and β-$NaMnO_2$ considering both experimental and optimized structures reported in [65]. (b) and (c) Range of DFT predicted NMR parameters for two mixed α/β-$NaMnO_2$ structures, proposed in [65], that contain twin boundaries between structural domains of both phases. Na(1) and Na(2) feature similar Mn-O-Na interactions, and only differ in the spatial arrangement of the atoms around the sodium ion, leading to similar isotropic shifts, δ_{iso}, and different shift anisotropy ($\Delta\delta$ and η) and quadrupolar parameters (C_q and η_q). The same argument holds true for the Na(β)/pseudo β and Na(α)/pseudo α sites, respectively. All DFT based NMR parameters were transcribed from [65] and used B3LYP functional with 20 and 35% Hartree-Fock exchange implemented in the CRYSTAL09 code [85]. (d)^{23}Na NMR parameters obtained obtained by fitting the extracted one-dimensional slices of the MAT spectrum shown in figure 6. Three resonances were assigned to β (β_1 and β_2) and α-"like" environments and two resonances were assigned to sites in the vicinity of a stacking fault (SF_1 and SF_2). The Na* environment corresponds to sodium ions in a different local environment in the orthorhombic sodium deficient phase shown in 2(c). Relative quantification of each sodium environment was obtained considering the fitted signal intensities of each site of spectrum recorded at 11.7 T, shown in figure 7. The observed shifts, $\delta_{obs} = \delta_{iso} + \delta_{QIS}$, were calculated considering an external magnetic field of 11.7 T.

References

[1] H. W. Spiess, 50th anniversary perspective: The importance of NMR spectroscopy to macromolecular science, Macromolecules 50 (5) (2017) 1761–1777.

[2] M. Edén, NMR studies of oxide-based glasses, Annual Reports Section" C"(Physical Chemistry) 108 (1) (2012) 177–221.

[3] R. Youngman, NMR spectroscopy in glass science: a review of the elements, Materials 11 (4) (2018) 476.

[4] R. Aleksis, F. Oleskovs, K. Jaudzems, J. Pahnke, H. Biverstål, Structural studies of amyloid-β peptides: Unlocking the mechanism of aggregation and the associated toxicity, Biochimie 140 (2017) 176–192.

[5] R. J. Messinger, M. Ménétrier, E. Salager, A. Boulineau, M. Duttine, D. Carlier, J.-M. Ateba Mba, L. Croguennec, C. Masquelier, D. Massiot, et al., Revealing defects in crystalline lithium-ion battery electrodes by solid-state NMR: applications to $LiVPO_4F$, Chemistry of Materials 27 (15) (2015) 5212–5221.

[6] B. F. Chmelka, Materializing opportunities for NMR of solids, Journal of Magnetic Resonance 306 (2019) 91–97.

[7] A. J. Rossini, A. Zagdoun, M. Lelli, A. Lesage, C. Coperet, L. Emsley, Dynamic nuclear polarization surface enhanced NMR spectroscopy, Accounts of chemical research 46 (9) (2013) 1942–1951.

[8] S. E. Ashbrook, Recent advances in solid-state NMR spectroscopy of quadrupolar nuclei, Physical Chemistry Chemical Physics 11 (32) (2009) 6892–6905.

[9] R. Tycko, Solid-state NMR studies of amyloid fibril structure, Annual review of physical chemistry 62 (2011) 279–299.

[10] D. L. Bryce, NMR crystallography: structure and properties of materials from solid-state nuclear magnetic resonance observables, IUCrJ 4 (4) (2017) 350–359.

[11] J. J. van der Klink, H. B. Brom, NMR in metals, metal particles and metal cluster compounds, Progress in Nuclear Magnetic Resonance Spectroscopy 36 (2) (2000) 89–201.

[12] W. Papawassiliou, A. Jaworski, A. J. Pell, J. H. Jang, Y. Kim, S.-C. Lee, H. J. Kim, Y. Alwahedi, S. Alhassan, A. Subrati, et al., Resolving Dirac electrons with broadband high-resolution NMR, Nature communications 11 (1) (2020) 1–7.

[13] W. Papawassiliou, J. P. Carvalho, N. Panopoulos, Y. Al Wahedi, V. K. S. Wadi, X. Lu, K. Polychronopoulou, J. B. Lee, S. Lee, C. Y. Kim, et al., Crystal and electronic facet analysis of ultrafine Ni_2P particles by solid-state NMR nanocrystallography, Nature Communications 12 (1) (2021) 1–11.

[14] A. J. Pell, G. Pintacuda, C. P. Grey, Paramagnetic NMR in solution and the solid state, Progress in nuclear magnetic resonance spectroscopy 111 (2019) 1–271.

[15] R. Pigliapochi, L. O'Brien, A. J. Pell, M. W. Gaultois, Y. Janssen, P. G. Khalifah, C. P. Grey, When Do Anisotropic Magnetic Susceptibilities Lead to Large NMR Shifts? Exploring Particle Shape Effects in the Battery Electrode Material $LiFePO_4$, Journal of the American Chemical Society 141 (33) (2019) 13089–13100.

[16] J. Kowalewski, D. Kruk, G. Parigi, NMR relaxation in solution of paramagnetic complexes: recent theoretical progress for $S \geq 1$, Advances in inorganic chemistry 57.

[17] M. Alla, E. Lippmaa, Resolution limits in magic-angle rotation NMR spectra of polycrystalline solids, Chemical Physics Letters 87 (1) (1982) 30–33.

[18] A. Kubo, T. P. Spaniol, T. Terao, The effect of bulk magnetic susceptibility on solid state NMR spectra of paramagnetic compounds, Journal of Magnetic Resonance 133 (2) (1998) 330–340.

[19] N. P. Wickramasinghe, M. A. Shaibat, C. R. Jones, L. B. Casabianca, A. C. De Dios, J. S. Harwood, Y. Ishii, Progress in ^{13}C and ^{1}H solid-state nuclear magnetic resonance for paramagnetic systems under very fast magic angle spinning, The Journal of chemical physics 128 (5) (2008) 02B610.

[20] G. Kervern, G. Pintacuda, Y. Zhang, E. Oldfield, C. Roukoss, E. Kuntz, E. Herdtweck, J.-M. Basset, S. Cadars, A. Lesage, et al., Solid-state NMR of a paramagnetic DIAD-FeII catalyst: Sensitivity, resolution enhancement, and structure-based assignments, Journal of the American Chemical Society 128 (41) (2006) 13545–13552.

[21] A. J. Pell, R. J. Clément, C. P. Grey, L. Emsley, G. Pintacuda, Frequency-stepped acquisition in nuclear magnetic resonance spectroscopy under magic angle spinning, The Journal of chemical physics 138 (11) (2013) 114201.

[22] A. W. MacGregor, L. A. O'Dell, R. W. Schurko, New methods for the acquisition of ultra-wideline solid-state NMR spectra of spin-1/2 nuclides, Journal of Magnetic Resonance 208 (1) (2011) 103 – 113, ISSN 1090-7807.

[23] L. A. O'Dell, R. W. Schurko, Fast and simple acquisition of solid-state ^{14}N NMR spectra with signal enhancement via population transfer, Journal of the American Chemical Society 131 (19) (2009) 6658–6659.

[24] Y. Tong, Nuclear spin-echo Fourier-transform mapping spectroscopy for broad NMR lines in solids, Journal of Magnetic Resonance, Series A 119 (1) (1996) 22–28.

[25] N. P. Wickramasinghe, Y. Ishii, Sensitivity enhancement, assignment, and distance measurement in ^{13}C solid-state NMR spectroscopy for paramagnetic systems under fast magic angle spinning, Journal of Magnetic Resonance 181 (2) (2006) 233–243.

[26] S. K. K. Swamy, A. Karczmarska, M. Makowska-Janusik, A. Kassiba, J. Dittmer, Solid-state NMR correlation experiments and distance measurements in paramagnetic metalorganics exemplified by Cu-cyclam, ChemPhysChem 14 (9) (2013) 1864–1870.

[27] J. Z. Hu, D. Alderman, C. Ye, R. Pugmire, D. Grant, An isotropic chemical shift-chemical shift anisotropy magic-angle slow-spinning 2D NMR experiment, Journal of Magnetic Resonance, Series A 105 (1) (1993) 82–87.

[28] M. Crozet, M. Chaussade, M. Bardet, L. Emsley, B. Lamotte, J.-M. Mouesca, Carbon-13 Solid-State NMR Studies on Synthetic Model Compounds of [4Fe$^-$ 4S] Clusters in the 2^+ State, The Journal of Physical Chemistry A 104 (44) (2000) 9990–10000.

[29] O. N. Antzutkin, S. Shekar, M. H. Levitt, Two-dimensional sideband separation in magic-angle-spinning NMR, Journal of Magnetic Resonance, Series A 115 (1) (1995) 7–19.

[30] I. Hung, L. Zhou, F. Pourpoint, C. P. Grey, Z. Gan, Isotropic high field NMR spectra of Li-ion battery materials with anisotropy > 1 MHz, Journal of the American Chemical Society 134 (4) (2012) 1898–1901.

[31] J. Xu, D. H. Lee, R. J. Clément, X. Yu, M. Leskes, A. J. Pell, G. Pintacuda, X.-Q. Yang, C. P. Grey, Y. S. Meng, Identifying the critical role of Li substitution in P2-$Na_x[Li_yNi_zMn_{1-y-z}]O_2$ ($0 < x, y, z < 1$) intercalation cathode materials for high-energy Na-ion batteries, Chemistry of Materials 26 (2) (2014) 1260–1269.

[32] M. Garwood, L. DelaBarre, The return of the frequency sweep: designing adiabatic pulses for contemporary NMR, Journal of magnetic resonance 153 (2) (2001) 155–177.

[33] Ē. Kupcče, R. Freeman, Stretched adiabatic pulses for broadband spin inversion, Journal of Magnetic Resonance, Series A 117 (2) (1995) 246–256.

[34] Y. A. Tesiram, M. R. Bendall, Universal equations for linear adiabatic pulses and characterization of partial adiabaticity, Journal of Magnetic Resonance 156 (1) (2002) 26–40.

[35] J. Baum, R. Tycko, A. Pines, Broadband and adiabatic inversion of a two-level system by phase-modulated pulses, Physical Review A 32 (6) (1985) 3435.

[36] E. Kupcče, R. Freeman, Adiabatic pulses for wideband inversion and broadband decoupling, Journal of magnetic resonance. Series A (Print) 115 (2) (1995) 273–276.

[37] A. J. Pell, G. Pintacuda, Broadband solid-state MAS NMR of paramagnetic systems, Progress in nuclear magnetic resonance spectroscopy 84 (2015) 33–72.

[38] J. P. Carvalho, A. J. Pell, Frequency-swept adiabatic pulses for broadband solid-state MAS NMR, Journal of Magnetic Resonance 324 (2021) 106911.

[39] J. Koppe, M. Bußkamp, M. R. Hansen, Frequency-Swept Ultra-Wideline Magic-Angle Spinning NMR Spectroscopy, The Journal of Physical Chemistry A 125 (25) (2021) 5643–5649.

[40] A. R. Altenhof, M. J. Jaroszewicz, A. W. Lindquist, L. D. Foster, S. L. Veinberg, R. W. Schurko, Practical aspects of recording ultra-wideline NMR patterns under magic-angle spinning conditions, The Journal of Physical Chemistry C 124 (27) (2020) 14730–14744.

[41] L. A. O'Dell, R. W. Schurko, QCPMG using adiabatic pulses for faster acquisition of ultra-wideline NMR spectra, Chemical Physics Letters 464 (1-3) (2008) 97–102.

[42] L. A. O'Dell, A. J. Rossini, R. W. Schurko, Acquisition of ultra-wideline

NMR spectra from quadrupolar nuclei by frequency stepped WURST–QCPMG, Chemical physics letters 468 (4-6) (2009) 330–335.

[43] R. W. Schurko, Ultra-wideline solid-state NMR spectroscopy, Accounts of chemical research 46 (9) (2013) 1985–1995.

[44] J. Koppe, M. R. Hansen, Minimizing lineshape distortions in static ultra-wideline nuclear magnetic resonance of half-integer spin quadrupolar nuclei, The Journal of Physical Chemistry A 124 (21) (2020) 4314–4321.

[45] V. Vitzthum, M. A. Caporini, S. Ulzega, G. Bodenhausen, Broadband excitation and indirect detection of nitrogen-14 in rotating solids using Delays Alternating with Nutation (DANTE), Journal of Magnetic Resonance 212 (1) (2011) 234–239.

[46] A. J. Pell, K. J. Sanders, S. Wegner, G. Pintacuda, C. P. Grey, Low-power broadband solid-state MAS NMR of ^{14}N, The Journal of Chemical Physics 146 (19) (2017) 194202.

[47] R. Aleksis, A. J. Pell, Low-power synchronous helical pulse sequences for large anisotropic interactions in MAS NMR: Double-quantum excitation of ^{14}N, The Journal of Chemical Physics 153 (24) (2020) 244202.

[48] S. Antonijevic, S. Wimperis, Separation of quadrupolar and chemical/paramagnetic shift interactions in two-dimensional ^{2}H (I= 1) nuclear magnetic resonance spectroscopy, The Journal of chemical physics 122 (4) (2005) 044312.

[49] B. J. Walder, K. K. Dey, M. C. Davis, J. H. Baltisberger, P. J. Grandinetti, Two-dimensional NMR measurement and point dipole model prediction of paramagnetic shift tensors in solids, The Journal of chemical physics 142 (1) (2015) 014201.

[50] R. Aleksis, J. P. Carvalho, A. Jaworski, A. J. Pell, Artefact-free broadband 2D NMR for separation of quadrupolar and paramagnetic shift interactions, Solid state nuclear magnetic resonance 101 (2019) 51–62.

[51] R. Aleksis, A. J. Pell, Separation of quadrupolar and paramagnetic shift interactions in high-resolution nuclear magnetic resonance of spinning powders, The Journal of Chemical Physics 155 (9) (2021) 094202.

[52] L. Frydman, J. S. Harwood, Isotropic spectra of half-integer quadrupolar spins from bidimensional magic-angle spinning NMR, Journal of the American Chemical Society 117 (19) (1995) 5367–5368.

[53] Z. Gan, Isotropic NMR spectra of half-integer quadrupolar nuclei using satellite transitions and magic-angle spinning, Journal of the American Chemical Society 122 (13) (2000) 3242–3243.

[54] B. Blümich, P. Blümler, J. Jansen, Presentation of sideband envelopes by two-dimensional one-pulse (TOP) spectroscopy, Solid state nuclear magnetic resonance 1 (2) (1992) 111–113.

[55] M. C. Davis, K. M. Shookman, J. D. Sillaman, P. J. Grandinetti, TOPPASS: A processing algorithm to reduce 2D PASS acquisition time, Journal of Magnetic Resonance 210 (1) (2011) 51–58.

[56] B. J. Walder, K. K. Dey, D. C. Kaseman, J. H. Baltisberger, P. J. Grandinetti, Sideband separation experiments in NMR with phase incremented echo train acquisition, The Journal of Chemical Physics 138 (17) (2013) 174203.

[57] J. P. Carvalho, A. Jaworski, M. J. Brady, A. J. Pell, Separation of quadrupolar and paramagnetic shift interactions with TOP-STMAS/MQMAS in solid-state lighting phosphors, Magnetic Resonance in Chemistry 58 (11) (2020) 1055–1070.

[58] S. Prasad, H.-T. Kwak, T. Clark, P. J. Grandinetti, A simple technique for determining nuclear quadrupole coupling constants with RAPT solid-state NMR spectroscopy, Journal of the American Chemical Society 124 (18) (2002) 4964–4965.

[59] H.-T. Kwak, S. Prasad, T. Clark, P. J. Grandinetti, Enhancing sensitivity of quadrupolar nuclei in solid-state NMR with multiple rotor assisted population transfers, Solid state nuclear magnetic resonance 24 (2-3) (2003) 71–77.

[60] J. Lee, I. D. Seymour, A. J. Pell, S. E. Dutton, C. P. Grey, A systematic study of ^{25}Mg NMR in paramagnetic transition metal oxides: applications to Mg-ion battery materials, Physical Chemistry Chemical Physics 19 (1) (2017) 613–625.

[61] H. Xia, X. Zhu, J. Liu, Q. Liu, S. Lan, Q. Zhang, X. Liu, J. K. Seo, T. Chen, L. Gu, et al., A monoclinic polymorph of sodium birnessite for ultrafast and ultrastable sodium ion storage, Nature communications 9 (1) (2018) 1–10.

[62] R. J. Clément, P. G. Bruce, C. P. Grey, manganese-based P2-type transition metal oxides as sodium-ion battery cathode materials, Journal of The Electrochemical Society 162 (14) (2015) A2589.

[63] R. J. Clément, J. Billaud, A. Robert Armstrong, G. Singh, T. Rojo, P. G. Bruce, C. P. Grey, Structurally stable Mg-doped P2-$Na_{2/3}Mn_{1-y}Mg_yO_2$ sodium-ion battery cathodes with high rate performance: insights from electrochemical, NMR and diffraction studies, Energy Environ. Sci. 9 (2016) 3240–3251.

[64] J. Billaud, R. J. Clément, A. R. Armstrong, J. Canales-Vázquez, P. Rozier, C. P. Grey, P. G. Bruce, β-$NaMnO_2$: a high-performance cathode for sodium-ion batteries, Journal of the American Chemical Society 136 (49) (2014) 17243–17248.

[65] R. J. Clément, D. S. Middlemiss, I. D. Seymour, A. J. Ilott, C. P. Grey, Insights into the nature and evolution upon electrochemical cycling of planar defects in the β-$NaMnO_2$ Na-ion battery cathode: An NMR and first-principles density functional theory approach, Chemistry of Materials 28 (22) (2016) 8228–8239.

[66] A. M. Abakumov, A. A. Tsirlin, I. Bakaimi, G. Van Tendeloo, A. Lappas, Multiple twinning as a structure directing mechanism in layered rock-salt-type oxides: $NaMnO_2$ polymorphism, redox potentials, and magnetism, Chemistry of Materials 26 (10) (2014) 3306–3315.

[67] J. Rodriguez-Carvajal, FULLPROF: a program for Rietveld refinement and pattern matching analysis, in: satellite meeting on powder diffraction of the XV congress of the IUCr, vol. 127, Toulouse, France:[sn], 1990.

[68] Z. Yao, H.-T. Kwak, D. Sakellariou, L. Emsley, P. J. Grandinetti, Sensitivity enhancement of the central transition NMR signal of quadrupolar nuclei under magic-angle spinning, Chemical Physics Letters 327 (1-2) (2000) 85–90.

[69] S. E. Ashbrook, S. Wimperis, High-resolution NMR of quadrupolar nuclei in solids: the satellite-transition magic angle spinning (STMAS) experiment, Progress in Nuclear Magnetic Resonance Spectroscopy 45 (1-2) (2004) 53–108.

[70] T. O. Pennanen, J. Vaara, Nuclear magnetic resonance chemical shift in an arbitrary electronic spin state, Physical review letters 100 (13) (2008) 133002.

[71] Z. Yao, H.-T. Kwak, D. Sakellariou, L. Emsley, P. J. Grandinetti, Sensitivity enhancement of the central transition NMR signal of quadrupolar nuclei under magic-angle spinning, Chemical Physics Letters 327 (1) (2000) 85–90, ISSN 0009-2614, doi:https://doi.org/10.1016/S0009-2614(00)00805-8.

[72] S. Prasad, T. M. Clark, R. Sharma, H.-T. Kwak, P. J. Grandinetti, H. Zimmermann, A combined ^{17}O RAPT and MQ-MAS NMR study of l-leucine, Solid State Nuclear Magnetic Resonance 29 (1-3) (2006) 119–124.

[73] J. T. Ash, P. J. Grandinetti, Solid-state NMR characterization of ^{69}Ga and ^{71}Ga in crystalline solids, Magnetic Resonance in Chemistry 44 (9) (2006) 823–831, doi:https://doi.org/10.1002/mrc.1841.

[74] I. Hung, J. Trébosc, G. L. Hoatson, R. L. Vold, J.-P. Amoureux, Z. Gan, Q-shear transformation for MQMAS and STMAS NMR spectra, Journal of Magnetic Resonance 201 (1) (2009) 81–86.

[75] L. Kobera, J. Brus, P. Klein, J. Dedecek, M. Urbanova, Biaxial Q-shearing] of ^{27}Al 3QMAS NMR spectra: Insight into the structural disorder of framework aluminosilicates, Solid state nuclear magnetic resonance 57 (2014) 29–38.

[76] P. Blümler, J. Jansen, B. Blümich, Two-dimensional one-pulse rotational echo spectra, Solid State Nuclear Magnetic Resonance 3 (4) (1994) 237–240.

[77] P. J. Grandinetti, J. T. Ash, N. M. Trease, Symmetry pathways in solid-state NMR., Progress in Nuclear Magnetic Resonance Spectroscopy 59 (2) (2010) 121–196.

[78] D. States, R. Haberkorn, D. Ruben, A 2D NMR experiment with pure absorption phase in four quadrants, J. Magn. Res. 48 (1982) 286–292.

[79] M. Bak, J. T. Rasmussen, N. C. Nielsen, SIMPSON: a general simulation program for solid-state NMR spectroscopy, Journal of magnetic resonance 213 (2) (2011) 366–400.

[80] D. Alderman, M. S. Solum, D. M. Grant, Methods for analyzing spectroscopic line shapes. NMR solid powder patterns, The Journal of chemical physics 84 (7) (1986) 3717–3725.

[81] D. S. Middlemiss, A. J. Ilott, R. J. Clement, F. C. Strobridge, C. P. Grey, Density functional theory-based bond pathway decompositions of hyperfine shifts: Equipping solid-state NMR to characterize atomic environments in paramagnetic materials, Chemistry of Materials 25 (9) (2013) 1723–1734.

[82] I. Hung, Z. Gan, A magic-angle turning NMR experiment for separating spinning sidebands of half-integer quadrupolar nuclei, Chemical Physics

Letters 496 (1-3) (2010) 162–166.

[83] T. Nakai, D. Kuwahara, Spinning sideband summation for quadrupole MAS NMR spectra using a magic-angle turning technique, Chemical physics letters 249 (3-4) (1996) 205–209.

[84] D. Massiot, V. Montouillout, F. Fayon, P. Florian, C. Bessada, Order-resolved sideband separation in magic angle spinning NMR of half integer quadrupolar nuclei, Chemical physics letters 272 (3-4) (1997) 295–300.

[85] R. Dovesi, R. Orlando, B. Civalleri, C. Roetti, V. R. Saunders, C. M. Zicovich-Wilson, CRYSTAL: a computational tool for the ab initio study of the electronic properties of crystals, Zeitschrift für Kristallographie - Crystalline Materials 220 (5-6) (2005) 571–573.